 CMES, vol.3, no.6, pp.717-730, 2002

Analysis of Elastodynamic Deformations near a Crack/Notch Tip by the Meshless Local Petrov-Galerkin (MLPG) Method

R. C. Batra[1] **and H.-K. Ching**[1]

Abstract: The Meshless Local Petrov-Galerkin (MLPG) method is used to analyze transient deformations near either a crack or a notch tip in a linear elastic plate. The local weak formulation of equations governing elastodynamic deformations is derived. It results in a system of coupled ordinary differential equations which are integrated with respect to time by a Newmark family of methods. Essential boundary conditions are imposed by the penalty method. The accuracy of the MLPG solution is established by comparing computed results for one-dimensional wave propagation in a rod with the analytical solution of the problem. Results are then computed for the following two problems: a rectangular plate with a central crack with plate edges parallel to the crack axis loaded in tension, and a double edge-notched plate with the edge between the notches loaded by compressive tractions. Stresses at points near the crack/notch tip computed from the MLPG solution are found to agree well with those obtained from either the analytical or the finite element solution of the same problem. The index of stress singularity is ascertained from a plot of log (stress) vs. $\log(r)$ where r is the distance from the crack tip. It is found that, for the double-edge notched plate, the mode-mixity of deformations near a notch-tip in an orthotropic plate can be adjusted by suitably varying the in-plane moduli of the material of the plate. The variation of shear stress with r exhibits a boundary layer effect near $r = 0$.

1 Introduction

The meshless method has attracted considerable attention in the past two decades due to the flexibility of placing nodes in the domain of study. Atluri and Zhu (1998) have proposed a meshless method which requires no background mesh to evaluate numerically various integrals appearing in the local weak formulation of the problem. Atluri et al. (1999) have pointed out that the Galerkin approximation can also be adopted that leads to a symmetric stiffness matrix. Atluri and Zhu (2000) solved elastostatic problems by the MLPG method, and Lin and Atluri (2000) introduced the upwinding scheme to analyze steady convection-diffusion problems. Ching and Batra (2001) enriched the polynomial basis functions with those appropriate to describe singular deformation fields near a crack tip and used the diffraction criterion to find stress intensity factors, the J-integrals and singular stress fields near a crack tip. Gu and Liu (2001) used the Newmark family of methods to study forced vibrations of a beam. The problem of bending of a thin plate has been studied by Long and Atluri (2002). Warlock et al. (2002) have analyzed elastostatic deformations of a material compressed in a rough rectangular cavity analytically by the Laplace transformation technique and numerically by the MLPG method. Atluri and Shen (2002a,b) have demonstrated the use of different weight functions and have compared their performance with that of the Galerkin finite element method. By choosing a Heaviside step function as the test function, they eliminated the domain integration in the local weak form. Thus only boundary integrals over local subdomains remained in the local weak form. For elastostatic problems, this was shown to be more efficient than both the finite element and the boundary element methods.

The paper is organized as follows. Section 2 gives the MLPG formulation including the local weak form, the moving least squares approximation, the discrete governing equations and the time integration scheme. Calculations of the dynamic stress intensity factors from the near-tip stress fields are also described. Numerical examples are presented in Section 3. The MLPG results are compared with either analytical or finite element solutions. Section 4 summarizes the conclusions.

[1] Department of Engineering Science and Mechanics, MC 0219
Virginia Polytechnic Institute and State University
Blacksburg, VA 24061

2 Formulation of the Problem

2.1 Governing equations

For a plane linear elastodynamic problem on domain Ω bounded by the boundary Γ, governing equations in rectangular Cartesian coordinates are

$$\sigma_{ij,j}+b_i=\rho\ddot{u}_i, \text{ in } \Omega, \ (i,j=1,2), \tag{1}$$

$$\sigma_{ij}=\lambda\varepsilon_{kk}\delta_{ij}+2\mu\varepsilon_{ij}, \text{ in } \Omega, \tag{2}$$

$$\varepsilon_{ij}=(u_{i,j}+u_{j,i})/2, \text{ in } \Omega. \tag{3}$$

Here ρ is the mass density, u_i the displacement, t the time, $\ddot{u}_i=\partial^2 u_i/\partial t^2$ the acceleration, σ_{ij} the stress tensor, ε_{ij} the infinitesimal strain tensor, b_i density of the body force vector, λ and μ are Lame' constants for the material of the body, $u_{i,j}=\partial u_i/\partial x_j$, $\mathbf{x}$ gives the present position of a material particle, and a repeated index implies summation over the range of the index. Equations (1)-(3) are supplemented with the following initial and boundary conditions:

$$\mathbf{u}(\mathbf{x},t_0)=\mathbf{u}_0(\mathbf{x}), \quad \mathbf{x}\in\Omega, \tag{4}$$

$$\dot{\mathbf{u}}(\mathbf{x},t_0)=\dot{\mathbf{u}}_0(\mathbf{x}), \quad \mathbf{x}\in\Omega, \tag{5}$$

$$u_i=\overline{u}_i, \text{ on } \Gamma_u, \tag{6}$$

$$t_i\equiv\sigma_{ij}n_j=\overline{t}_i, \text{ on } \Gamma_t. \tag{7}$$

Here $\overline{u}_i,\overline{t}_i,\mathbf{u}_0$ and $\dot{\mathbf{u}}_0$ denote the prescribed displacements, tractions, initial displacements and initial velocities, respectively, n_j is the unit outward normal to Γ, and Γ_u and Γ_t are complementary parts of Γ where essential and natural boundary conditions are prescribed.

2.2 Implementation of the MLPG method

Taking the inner product of (1) with $\mathbf{v}$ and of (6) with $\alpha\mathbf{v}$, and integrating the resulting equations over Ω_s and Γ_{su} respectively, we obtain

$$\int_{\Omega_s}(\sigma_{ij,j}-\rho\ddot{u}_i+b_i)\nu_i d\Omega-\int_{\Gamma_{su}}\alpha(u_i-\overline{u}_i)\nu_i d\Gamma=0, \tag{8}$$

where $\Gamma_{su}=\Gamma_s\cap\Gamma_u$, Γ_s is the boundary of the local domain $\Omega_s\subset\Omega$ and α is a penalty parameter used to satisfy the essential boundary conditions. For eqn. (8) to be dimensionally correct, α must have units of Force/(Length)^3. The penalty parameter α may vary from point to point but is usually taken to be a constant with magnitude much larger than λ/L where L is a typical dimension of the body. Henceforth we take α to be a constant.

Integrating the first term on the left side of (8) by parts, and using natural boundary condition (7) we obtain

$$\int_{\Omega_s}\rho\nu_i\ddot{u}_i d\Omega+\int_{\Omega_s}\nu_{i,j}\sigma_{ij}d\Omega+\alpha\int_{\Gamma_{su}}\nu_i u_i d\Gamma-\int_{\Gamma_{su}}\nu_i t_i d\Gamma$$
$$=\int_{\Gamma_{st}}\nu_i\overline{t}_i d\Gamma+\alpha\int_{\Gamma_{su}}\nu_i\overline{u}_i d\Gamma+\int_{\Omega_s}\nu_i b_i d\Omega, \tag{9}$$

where $\Gamma_{st}=\Gamma_s\cap\Gamma_t$, and ν_i is taken to vanish on $\partial\Omega_s-\Gamma_{su}-\Gamma_{st}$.

In the MLPG method, the displacement field is approximated by the moving least squares method (MLS). Details about the MLS approximation are given in the paper by Lancaster and Salkauskas (1981). For the sake of completeness, the MLS approximation is briefly described here. We consider the trial function $\mathbf{u}^h(\mathbf{x},t)$ over the domain Ω defined by

$$u_k^h(\mathbf{x},t)=\sum_{j=1}^{m}p_j(\mathbf{x})a_{jk}(\mathbf{x},t), \ k=1,2, \tag{10}$$

where the unknown coefficients $\mathbf{a}(\mathbf{x},t)$ are functions of the space coordinates $\mathbf{x}^T=[x_1,x_2]$ and time t, and $\mathbf{p}(\mathbf{x})$ is a complete monomial in $\mathbf{x}$ having m terms. The complete quadratic monomials basis functions in two-dimensions are

$$\mathbf{p}^T(\mathbf{x})=[1,x_1,x_2,(x_1)^2,x_1x_2,(x_2)^2]; \ m=6. \tag{11}$$

For each component of $\mathbf{u}$, the coefficients $\mathbf{a}(\mathbf{x},t)$ in (10) are obtained by minimizing J defined by

$$J=\sum_{i=1}^{n}w(\mathbf{x}-\mathbf{x}_i)[\mathbf{p}^T(\mathbf{x}_i)\mathbf{a}(\mathbf{x},t)-\hat{u}_i(t)]^2. \tag{12}$$

Here $\hat{u}_i$ is the fictitious value of a component of $\mathbf{u}^h$ at $\mathbf{x}=\mathbf{x}_i$, and n is the number of nodes in the domain of influence of $\mathbf{x}$ for which the weight functions $w(\mathbf{x}-\mathbf{x}_i)\neq 0$. Several different weight functions are given in Atluri and Shen (2002a,b); here, the following Gaussian weight function is used.

$$w(\mathbf{x}-\mathbf{x}_i)=\begin{cases}\dfrac{\exp\left[-\left(\frac{|\mathbf{x}-\mathbf{x}_i|}{c_i}\right)^{2k}\right]-\exp\left[-\left(\frac{r_i}{c_i}\right)^{2k}\right]}{1-\exp\left[-\left(\frac{r_i}{c_i}\right)^{2k}\right]}, & 0\le|\mathbf{x}-\mathbf{x}_i|\le r_i,\\ 0, & |\mathbf{x}-\mathbf{x}_i|>r_i.\end{cases} \tag{13}$$

Here r_i is the radius of the domain of influence for the weight function $w(\mathbf{x}-\mathbf{x}_i)$, and empirically determined

parameters c_i and k control its shape. We set $k=1$, $c_i=$ distance to the third nearest neighboring node from the node $\mathbf{x}_i$ with nodes equidistant from $\mathbf{x}_i$ counted once, and $r_i = 3.5c_i$.

The support of $w(\mathbf{x}-\mathbf{x}_i)$ is also called the domain of influence of node i, since node i affects the approximation within this domain but not outside of this domain. The domain of influence is usually a circle, but it does not extend outside of the boundary of domain Ω. The effect of a crack is represented by changes in the domains of influence of the nodes surrounding the crack. The diffraction criterion proposed by Organ et al. (1996) has been used by Ching and Batra (2001) to account for changes in the domain of influence caused by discontinuous fields across a crack; it is also employed here.

The stationarity of J in (12) with respect to $\mathbf{a}(\mathbf{x},t)$ leads to

$$\mathbf{a}(\mathbf{x},t) = \mathbf{A}^{-1}(\mathbf{x})\mathbf{B}(\mathbf{x})\hat{\mathbf{u}}(t), \tag{14}$$

with matrices $\mathbf{A}(\mathbf{x})$ and $\mathbf{B}(\mathbf{x})$ defined by

$$\mathbf{A}(\mathbf{x}) = \sum_{i=1}^{n} w(\mathbf{x}-\mathbf{x}_i)\mathbf{p}(\mathbf{x}_i)\mathbf{p}^T(\mathbf{x}_i), \tag{15}$$

$$\mathbf{B}(\mathbf{x}) = [w(\mathbf{x}-\mathbf{x}_1)\mathbf{p}(\mathbf{x}_1), w(\mathbf{x}-\mathbf{x}_2)\mathbf{p}(\mathbf{x}_2), \ldots, w(\mathbf{x}-\mathbf{x}_n)\mathbf{p}(\mathbf{x}_n)]. \tag{16}$$

By substituting from (14) into (10), we obtain the MLS approximant as

$$u_k^h(\mathbf{x},t) = \sum_{i=1}^{n}\sum_{j=1}^{m} p_j(\mathbf{x})[\mathbf{A}^{-1}(\mathbf{x})\mathbf{B}(\mathbf{x})]_{ji}\hat{u}_{ik}(t) = \sum_{i=1}^{n}\phi_i(\mathbf{x})\hat{u}_{ik}(t). \tag{17}$$

$\phi_i(\mathbf{x})$ is usually called the MLS shape function corresponding to node i. Substituting (17) into the local weak form (9) for each node gives the following discrete equations:

$$\mathbf{M}\ddot{\hat{\mathbf{u}}}(t) + \mathbf{K}\hat{\mathbf{u}}(t) = \mathbf{f}(t). \tag{18}$$

The "mass" matrix $\mathbf{M}$, the "stiffness" matrix $\mathbf{K}$, and the "load" vector $\mathbf{f}$ are given by

$$\mathbf{M}_{ij} = \int_{\Omega_s} \rho\phi_j \mathbf{v}(\mathbf{x},\mathbf{x}_i)d\Omega, \quad i,j=1,2,\ldots,n, \tag{19}$$

$$\mathbf{K}_{ij} = \int_{\Omega_s} \varepsilon_\nu(\mathbf{x},\mathbf{x}_i)\mathbf{D}\mathbf{B}_j d\Omega + \alpha\int_{\Gamma_{su}} \mathbf{v}(\mathbf{x},\mathbf{x}_i)\mathbf{S}\phi_j d\Omega - \int_{\Gamma_{su}} \mathbf{v}(\mathbf{x},\mathbf{x}_i)\mathbf{N}\mathbf{D}\mathbf{B}_j\mathbf{S}d\Gamma, \tag{20}$$

$$\mathbf{f}_i = \int_{\Gamma_{st}} \mathbf{v}(\mathbf{x},\mathbf{x}_i)\bar{\mathbf{t}}d\Gamma + \alpha\int_{\Gamma_{su}} \mathbf{v}(\mathbf{x},\mathbf{x}_i)\mathbf{S}\bar{\mathbf{u}}d\Gamma + \int_{\Omega_s} \mathbf{v}(\mathbf{x},\mathbf{x}_i)\mathbf{b}d\Omega. \tag{21}$$

The matrices ε_ν, $\mathbf{D}$, $\mathbf{B}_j$, $\mathbf{S}$, and $\mathbf{N}$ are given below.

$$\varepsilon_\nu = \begin{bmatrix} \varepsilon_{11}^{(1)} & \varepsilon_{22}^{(1)} & 2\varepsilon_{12}^{(1)} \\ \varepsilon_{11}^{(2)} & \varepsilon_{22}^{(2)} & 2\varepsilon_{12}^{(2)} \end{bmatrix}, \tag{22}$$

$$\mathbf{B}_j = \begin{bmatrix} \phi_{j,1} & 0 \\ 0 & \phi_{j,2} \\ \phi_{j,2} & \phi_{j,1} \end{bmatrix}, \tag{23}$$

$$\mathbf{N} = \begin{bmatrix} n_1 & 0 & n_2 \\ 0 & n_2 & n_1 \end{bmatrix}, \tag{24}$$

$$\mathbf{D} = \frac{\overline{E}}{1-\overline{\nu}^2}\begin{bmatrix} 1 & \overline{\nu} & 0 \\ \overline{\nu} & 1 & 0 \\ 0 & 0 & (1-\overline{\nu})/2 \end{bmatrix}, \tag{25}$$

$$\overline{E} = \begin{cases} E & \text{for plane stress deformations,} \\ E/(1-\nu^2) & \text{for plane strain deformations,} \end{cases} \tag{26}$$

$$\overline{\nu} = \begin{cases} \nu & \text{for plane stress deformations,} \\ \nu/(1-\nu) & \text{for plane strain deformations,} \end{cases} \tag{27}$$

$$\mathbf{S} = \begin{bmatrix} S_1 & 0 \\ 0 & S_2 \end{bmatrix}, \; S_i = \begin{cases} 1 & \text{if } \mathbf{x}\in\Gamma_u, \\ 0 & \text{if } \mathbf{x}\notin\Gamma_u. \end{cases} \tag{28}$$

$E = \mu(3\lambda+2\mu)/(\lambda+\mu)$ is Young's modulus, and $\nu = \lambda/2(\lambda+\mu)$ is Poisson's ratio. Superscripts (1) and (2) signify, respectively, the quantity derived from two linearly independent test functions $\mathbf{v}^{(1)}$ and $\mathbf{v}^{(2)}$; a possibility is

$$\mathbf{v} = \begin{bmatrix} v & 0 \\ 0 & v \end{bmatrix}. \tag{29}$$

Here we take $v(\mathbf{x},\ \mathbf{x}_i) = w(\mathbf{x}-\mathbf{x}_i)$. Note that the "mass" matrix is not symmetric; the choice $v(\mathbf{x},\ \mathbf{x}_i) = \phi_i(\mathbf{x})$ will result in symmetric $\mathbf{M}$ and $\mathbf{K}$. The mass matrix can be

diagonalized by the row-sum technique to obtain

$$\mathbf{M}_{ii} = \sum_{j=1}^{n} \int_{\Omega_s} \rho\phi_j \mathbf{v}(\mathbf{x},\mathbf{x}_i) d\Omega, \text{ (no sum on } i\text{)},$$
$$\mathbf{M}_{ij} = 0, \; i \neq j. \tag{30}$$

For a 2-dimensional problem, $\mathbf{M}$ and $\mathbf{K}$ are $2n \times 2n$ matrices, where n is the total number of nodes in the problem.

Initial values of $\hat{\mathbf{u}}_i$ and $\dot{\hat{\mathbf{u}}}_i$ are derived from (4) and (5) as follows. The function $\mathbf{u}(\mathbf{x},t_0)$ is replaced by $\mathbf{u}^h(\mathbf{x},t_0)$, the inner product of both sides is taken with the function $\rho\mathbf{v}(\mathbf{x},\mathbf{x}_i)$, and the resulting equations are integrated over the local domain Ω_s. The result is

$$\mathbf{M}\hat{\mathbf{u}}(0) = \mathbf{F}^0, \tag{31}$$
$$\mathbf{M}\dot{\hat{\mathbf{u}}}(0) = \mathbf{G}^0, \tag{32}$$

where

$$\mathbf{F}_i^0 = \int_{\Omega_s} \rho\mathbf{u}_0(\mathbf{x}) \cdot \mathbf{v}(\mathbf{x},\mathbf{x}_i) d\Omega, \tag{33}$$
$$\mathbf{G}_i^0 = \int_{\Omega_s} \rho\dot{\mathbf{u}}_0(\mathbf{x}) \cdot \mathbf{v}(\mathbf{x},\mathbf{x}_i) d\Omega. \tag{34}$$

For null initial conditions, i.e., $\mathbf{u}_0 = \mathbf{0}$ and $\dot{\mathbf{u}}_0 = \mathbf{0}$, Eqs. (31) and (32) give $\hat{\mathbf{u}}(0) = \mathbf{0}$, $\dot{\hat{\mathbf{u}}}(0) = \mathbf{0}$.

For every $\mathbf{x}_i \in \Omega$ the local domain Ω_s is taken to be a circle, and equations (18), (31) and (32) are deduced. These equations form a system of coupled ordinary second-order differential equations for $\hat{\mathbf{u}}$ and algebraic equations for $\hat{\mathbf{u}}(0)$ and $\dot{\hat{\mathbf{u}}}(0)$. We choose a large number of local domains Ω_s so that their union contains Ω. Since local domains for different nodes may overlap, the sum of all elements of the global mass matrix will not, in general, equal the total mass of the body.

2.3 The time integration scheme

We use the Newmark family of methods (Newmark (1959)) to integrate the coupled second-order ordinary differential equations like (18). The recursive relations relating displacements and velocities at times t_n and t_{n+1} are

$$\hat{\mathbf{u}}_{n+1} = \hat{\mathbf{u}}_n + \Delta t\dot{\hat{\mathbf{u}}}_n + \frac{(\Delta t)^2}{2}\{(1-2\beta)\ddot{\hat{\mathbf{u}}}_n + 2\beta\ddot{\hat{\mathbf{u}}}_{n+1}\}, \tag{35}$$
$$\dot{\hat{\mathbf{u}}}_{n+1} = \dot{\hat{\mathbf{u}}}_n + \Delta t\{(1-\gamma)\ddot{\hat{\mathbf{u}}}_n + \gamma\ddot{\hat{\mathbf{u}}}_{n+1}\}, \tag{36}$$

where $\hat{\mathbf{u}}_n$, $\dot{\hat{\mathbf{u}}}_n$, and $\ddot{\hat{\mathbf{u}}}_n$ denote the displacements, velocities and accelerations, respectively, at time $t_n = n\Delta t$ and Δt is the uniform time interval between two time steps. Parameters β and γ control the stability and the accuracy of the time integration scheme. Values of β and γ for different methods are listed below:

$$\gamma = \frac{1}{2},\ \beta = \frac{1}{6}, \quad \text{Linear Acceleration Method;} \tag{37}$$
$$\gamma = \frac{1}{2},\ \beta = \frac{1}{4}, \quad \text{Constant Avg. Accel. Method;} \tag{38}$$
$$\gamma = \frac{3}{2},\ \beta = 1, \quad \text{Backward Difference Method;} \tag{39}$$
$$\gamma = \frac{1}{2},\ \beta = 0, \quad \text{Central-Difference Method.} \tag{40}$$

The Newmark family of methods is unconditionally stable if

$$\gamma \geq \frac{1}{2} \text{and} \beta \geq \frac{1}{4}\left(\frac{1}{2}+\gamma\right). \tag{41}$$

Thus the linear acceleration and the central difference methods are conditionally stable and the other two methods are unconditionally stable. The methods are second-order accurate and nondissipative for $\gamma = \frac{1}{2}$ and first-order accurate and dissipative for $\gamma \neq \frac{1}{2}$. For the conditionally stable methods,

$$\Delta t \leq \left(\frac{1}{4}-\beta\right)^{-1/2} / \omega_{\max} \tag{42}$$

where $\omega_{\max}$ is the maximum frequency of free vibration of the system. Thus for the central difference method, $\Delta t \leq 2/\omega_{\max}$. For a lumped mass matrix, the central difference method is explicit in the sense that the solution at time t_{n+1} can be found from that at time t_n without solving a system of algebraic equations.

Writing Eq. (18) at time $t_{n+1} = (n+1)\Delta t$, and substituting from (35) and (36) into (18) yield the following system of algebraic equations:

$$\hat{\mathbf{K}}_{n+1}\hat{\mathbf{u}}_{n+1} = \hat{\mathbf{F}}_{n+1}, \tag{43}$$

where

$$\hat{\mathbf{K}}_{n+1} = \mathbf{K}_{n+1} + a_1\mathbf{M}_{n+1}, \tag{44}$$
$$\hat{\mathbf{F}}_{n+1} = \mathbf{f}_{n+1} + \mathbf{M}_{n+1}\{a_1\hat{\mathbf{u}}_n + a_2\dot{\hat{\mathbf{u}}}_n + a_3\ddot{\hat{\mathbf{u}}}_n\}, \tag{45}$$
$$a_1 = \frac{1}{\beta(\Delta t)^2},\ a_2 = \frac{1}{\beta\Delta t},\ a_3 = \frac{1}{2\beta} - 1;\ \beta \neq 0. \tag{46}$$

Once $\hat{\mathbf{u}}_{n+1}$ has been computed from (43), $\ddot{\hat{\mathbf{u}}}_{n+1}$ and $\dot{\hat{\mathbf{u}}}_{n+1}$ can be obtained from

$$\ddot{\hat{\mathbf{u}}}_{n+1} = a_1\{\hat{\mathbf{u}}_{n+1} - \hat{\mathbf{u}}_n\} - a_2\dot{\hat{\mathbf{u}}}_n - a_3\ddot{\hat{\mathbf{u}}}_n, \tag{47}$$

$$\dot{\hat{\mathbf{u}}}_{n+1} = \dot{\hat{\mathbf{u}}}_n + (1-\gamma)\Delta t\ddot{\hat{\mathbf{u}}}_n + \gamma\Delta t\ddot{\hat{\mathbf{u}}}_{n+1}. \tag{48}$$

For $\beta = 0$, $\hat{\mathbf{u}}_{n+1}$ is first found from eqn. (35), $\ddot{\hat{\mathbf{u}}}$ from (18), and then $\dot{\hat{\mathbf{u}}}_{n+1}$ from (36).

2.4 Determination of the stress intensity factors

It has been shown by Ching and Batra (2001) that the stress intensity factors in linear elastic fracture mechanics can be determined from the plots on logarithmic scales of stresses near the crack tip computed from the MLPG solution versus distance from the crack tip. We determine here stress intensity factors for the transient problem from the near-tip stress fields. For dynamic deformations of an elastic body containing a stationary crack, the mode-I and the mode-II stress intensity factors can be determined from $K_I = \sqrt{2\pi r}\sigma_{22}(r,0,t)$ and $K_{II} = \sqrt{2\pi r}\sigma_{12}(r,0,t)$ (Miannay, 2001) where r is the distance straight ahead of the crack tip and should be taken within the singular-deformations dominated zone. In our computations, the distance r is taken within 2% of the crack length. At each time step, we plot $\ln|\sigma_{22}(r,0,t)|$ vs. $\ln r$ and $\ln|\sigma_{12}(r,0,t)|$ vs. $\ln r$, fit straight lines through the data by the least squares method, and compute K_I and K_{II} from the intercepts of these lines with the ordinates. Theoretically the slope of each line should equal $-1/2$, signifying the $1/\sqrt{r}$ singularity of stress fields near the crack tip.

3 Computation and Discussion of Results

3.1 One dimensional wave propagation

We have developed a computer code in Fortran based on the aforestated equations. To demonstrate the validity and accuracy of the code, the one-dimensional problem of wave propagation in a rod is studied first. A schematic sketch of the problem studied is shown in Fig. 1. The axial displacement u of a material point of the rod is given by

$$u(x,t) = \frac{8\bar{t}L}{E\pi^2}\left[\sum_{n=0}^{\infty}\frac{1}{(2n+1)^2}\cos\frac{\left(n+\frac{1}{2}\right)\pi ct}{L}\cdot \cos\frac{\left(n+\frac{1}{2}\right)\pi x}{L}\right] + \frac{\bar{t}}{E}x - \frac{\bar{t}L}{E}, \tag{49}$$

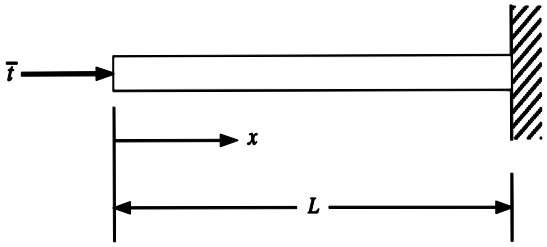

Figure 1 : A bar subjected to an impact force

where $c = \sqrt{E/\rho}$ is the wave speed.

When solving the problem by the MLPG method, we took $L = 20in$, $E = 30\times10^6$ psi, $\rho = 7.4\times10^{-4}\,lb\sec^2/in^4$, $A = 1in^2$, $\alpha = 10^9\,lb/in^3$ and $\bar{t}(t) = 100H(t)psi$ where $H(t)$ is the Heaviside step function. The bar was divided into 41 equally spaced nodes. All entries in the lumped mass matrix obtained from Eq. (30) were found to be positive. The time step size, Δt, equaled $0.5\mu s$ for the central difference method and $1\mu s$ for the other three methods. The maximum frequency, $\omega_{\max}$, was found to be 1.56 MH; thus Δt can at most equal $1.28\mu s$ for the explicit conditionally stable central difference method. However, for this method the value of Δt strongly depended upon the value of the penalty parameter. The maximum value of Δt that could be used to compute a stable solution rapidly decreased with an increase in the value of the penalty parameter, α. Numerical experiments indicated that α close to $10^4 E/L$ for the central difference method has a reasonable value of Δt.

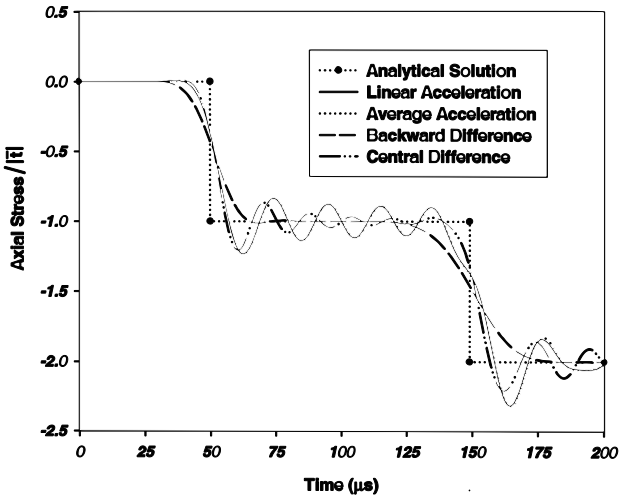

Figure 2 : Comparison with the analytical solution of the time history of the axial stress at the midpoint $(x = L/2)$ obtained by the four different integration methods

Figure 2 shows the comparison with the analytical solution of the time histories of the axial stress at the midpoint $(x = L/2)$ computed with different time integration schemes. The analytical value of the wave speed for the assumed material properties is $0.201\, in/\mu s$. It is clear that for each one of the four integration methods, the wave arrives at the midpoint prior to the theoretical value of $49.7\mu s$. This is to be expected because of the coupling among motions of different nodes induced by the stiffness matrix. Here a diagonal mass matrix is used; otherwise the mass matrix will also couple the motion of different nodes. The average acceleration and the linear acceleration methods predict identical values of the axial stress. Values of $\gamma > 1/2$ introduce damping into the computed solution; this is evident from the absence of oscillations in the solutions obtained with the backward difference method for which $\gamma = 3/2$. Each integration scheme correctly predicts doubling of the axial compressive stress when the wave reflected from the clamped end $(x = L)$ arrives at the midpoint. In order to see if decreasing the time step size will improve the accuracy of the computed results, we have plotted in Fig. 3 time histories of the axial stress at the midpoint obtained by taking $\Delta t = 0.4\mu s$ and $1.0\mu s$ and the backward difference method. These results indicate that, at least for the backward difference method, $\Delta t = 1\mu s$ is adequate. In

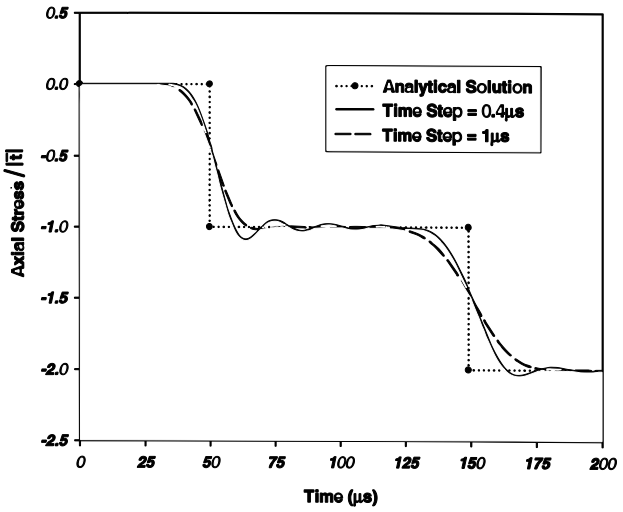

Figure 3 : Comparison with the analytical solution of the time history of the axial stress at the midpoint of the bar computed with two different time steps and by using the backward difference method

Fig. 4 we have compared at two locations time histories of the axial velocity obtained from the analytical solution with those computed with the backward difference method. The computed histories of the axial velocity exhibit oscillations of smaller amplitude than the computed histories of the axial stress. At $x = 0.25L$, oscillations die out and the computed axial velocity matches with the analytical value. It was found that the essential boundary condition prescribed at $x = L$ was very well satisfied.

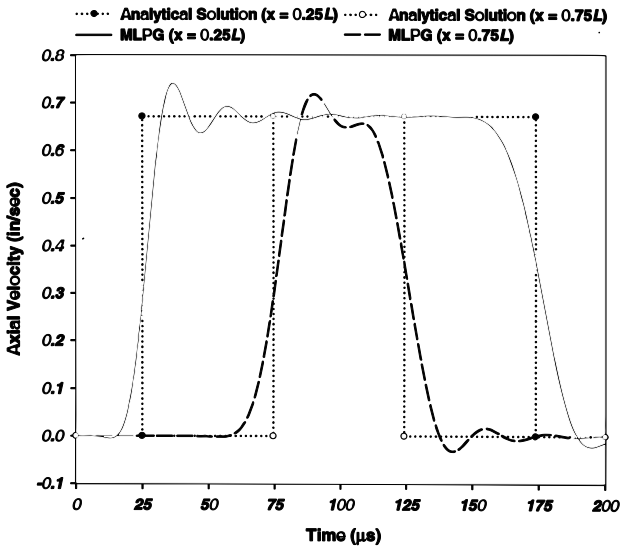

Figure 4 : Comparison with the analytical solution of the time history of the axial velocity at two different locations computed with the backward difference method

Time histories of the axial stress at $x = L/2$ computed with the lumped and the consistent mass matrices and the backward difference scheme were found to coincide with each other. Also, the evolutions of the axial stress at $x = L/2$ computed with two uniform arrangements of 41 and 101 nodes were identical suggesting that the nodal mesh of 41 uniformly placed nodes is adequate for analyzing this problem.

3.2 Rectangular plate with a central crack loaded in tension

We now analyze deformations of a rectangular plate with a centrally located crack, shown in Fig. 5, and loaded by axial tensile tractions applied at the top and the bottom surfaces. We set $\bar{t} = 0.4H(t)GPa$, $L = 52mm$, $D = 20mm$, $a = 12mm$, $\mu = 29.4GPa$, $\rho = 2450Kg/m^3$, $\alpha = 10^7 MPa/m$ and $\nu = 0.286$. A plane strain state of deformation is assumed to prevail in the plate and the

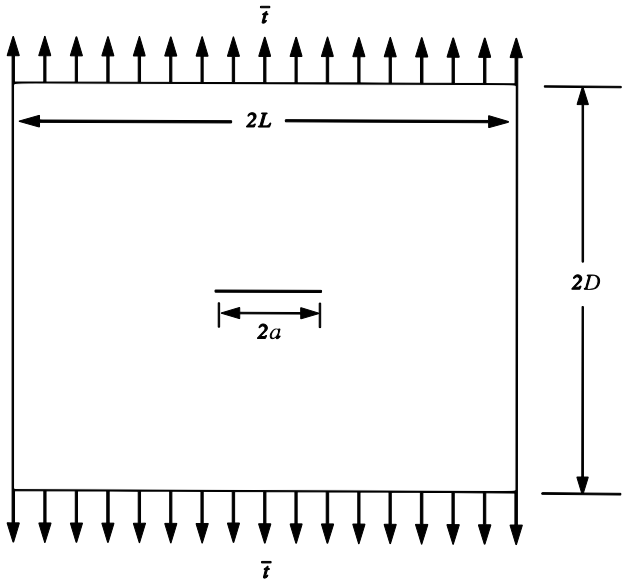

Figure 5 : A schematic sketch of the centrally cracked plate

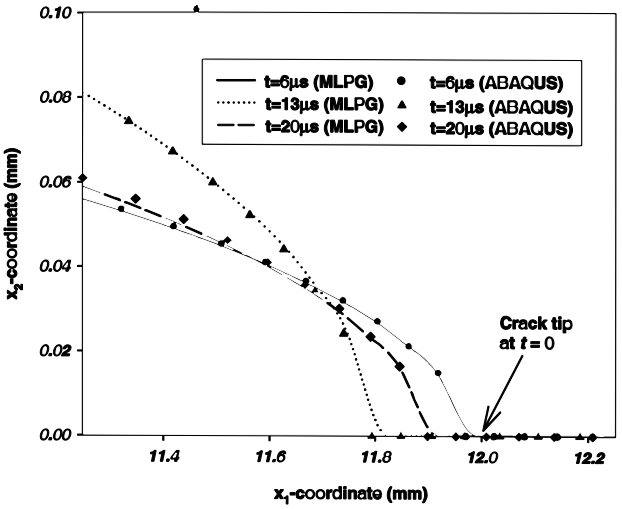

Figure 7 : At three different instants of time, deformed shape of the crack surface near the crack tip

diffraction criterion is used to account for discontinuous fields across the crack surface. Due to symmetry of the problem about the two centroidal axes, only a quadrant of the plate is modeled and discretized using 2534 nodes (see Fig. 6a) with a fine nodal mesh around the crack tip (cf. Fig. 6b). We use the backward difference method with $\Delta t = 4 \times 10^{-2} \mu s$ and compute results till $t = 20 \mu s$.

Figure 7 displays, at three different instants of time, the deformed crack surface obtained by both the MLPG and the finite element (FE) methods. In computing the FE solution with ABAQUS 6.11 the same nodal mesh as that in the MLPG method is employed. The two sets of computed results agree well with each other. Note that the material point located at the crack tip moves horizontally first to the right and then to the left while the upper and the lower boundaries of the plate are being pulled axially by the tensile tractions. The crack surfaces are comprised of the same material points since no opening or closing of the crack is considered. The time history of the stress intensity factor $K_I(t)$ normalized by $\bar{t}\sqrt{\pi a}$ is shown in Fig. 8. The MLPG solution is compared with the analytical solution of Baker (1962) for an infinite plate, the singular finite element solution of Nishioka and Atluri (1980) and the dual boundary element solution of Fedelinski et al. (1994) for a finite plate identical to the one studied here. The stress intensity factor K_I remains zero until the dilatational wave reaches the crack tip at approximately $t = 2.5 \mu s$. K_I attains the maximum value of 2.375 at $t = 11 \mu s$ and decreases subsequently; for the corresponding static problem, $K_I = 1.0361$ (e.g. see Anderson (1995)). It can be seen that there is a good agreement between the MLPG result and other available solutions. The time history of the order of singularity of the stress field near the crack tip is found to equal -0.48 which is close to the analytical value of -0.5. Figure 9 exhibits contours of the maximum principal stress normalized by $\bar{t}$ around the crack tip at $t = 13 \mu s$ for both the MLPG and the FE solutions. The two sets of solutions agree well with each other, and the maximum principal stress at the crack tip equals $45\bar{t}$.

3.3 Double edge-notched plate with the edge between the notches loaded in compression

3.3.1 Plate material isotropic

Kalthoff and Winkler (1987) proposed an experiment to study transient mode-II dominated deformations. It involves a double edge-notched plate with the edge between the two notches impacted by a fast moving cylindrical projectile of diameter equal to the distance between the notches. Here, we use the MLPG method to analyze this problem and approximate the action of the impactor by applying uniformly distributed compressive tractions on the impacted surface. Figure 10 shows a schematic sketch of the problem studied. We assume that a plane strain state of deformation prevails in the plate, and take Young's modulus $E = 210 GPa$,

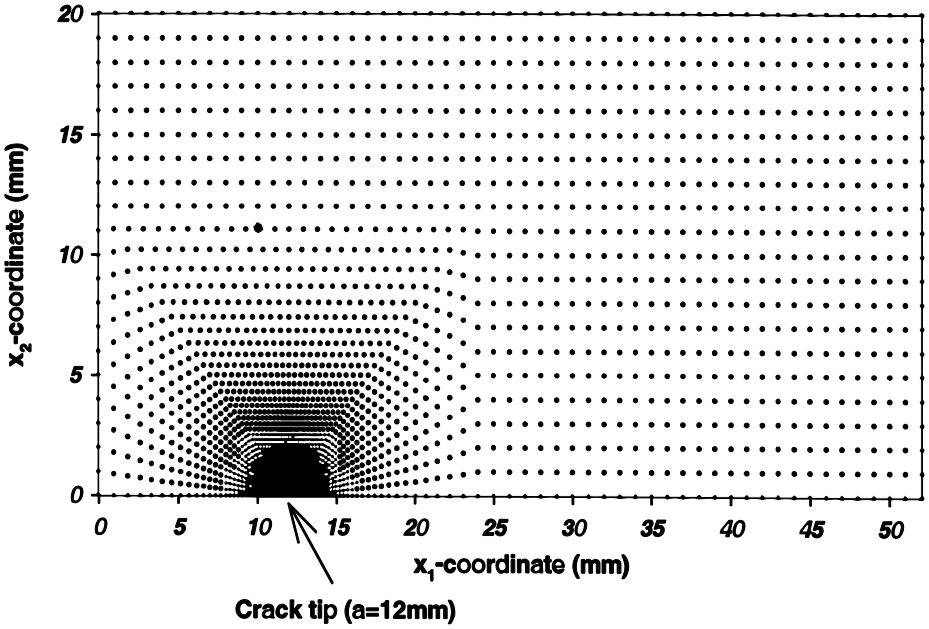

(a)

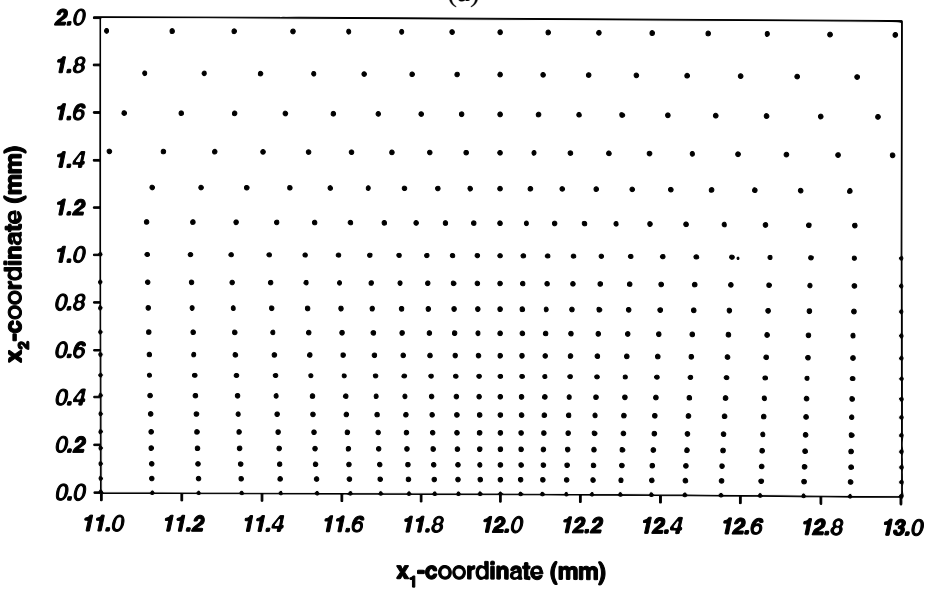

(b)

Figure 6 : (a) The nodal mesh for one quarter of the centrally cracked plate (b) The nodal mesh near the crack tip

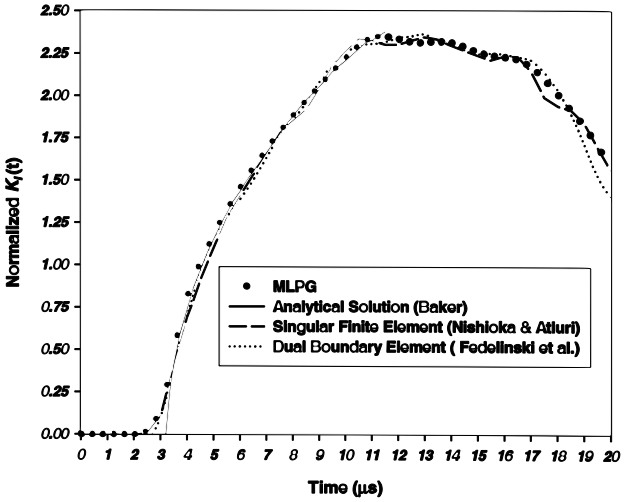

Figure 8 : The time history of the normalized stress intensity factor $K_I(t)$

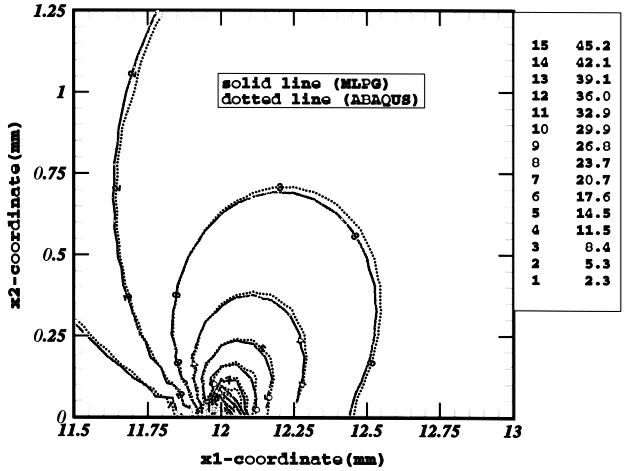

Figure 9 : Contours of the normalized maximum principal stress around the crack tip at $t = 13\mu$s

Poisson's ratio $\nu = 0.29$, mass density $\rho = 7833kg/m^3$, $\Delta t = 0.0625\mu s$, penalty parameter $\alpha = 10^8 MPa/m$, the radius of the circular notch tip $= 0.15mm$, the applied normal traction $\bar{t} = 200H(t)MPa$, and tangential traction on the impacted surface $= 0$. Because of symmetry of the problem about the horizontal centroidal plane, deformations of only the upper half of the plate are analyzed.

A nonuniform nodal mesh of 3632 nodes with 25 nodes on the surface of the circular notch tip is employed. The diffraction criterion is used to account for the discontinuous deformation fields across the notch. Coupled ordinary differential equations obtained from the local symmetric weak formulation of the governing partial differ-

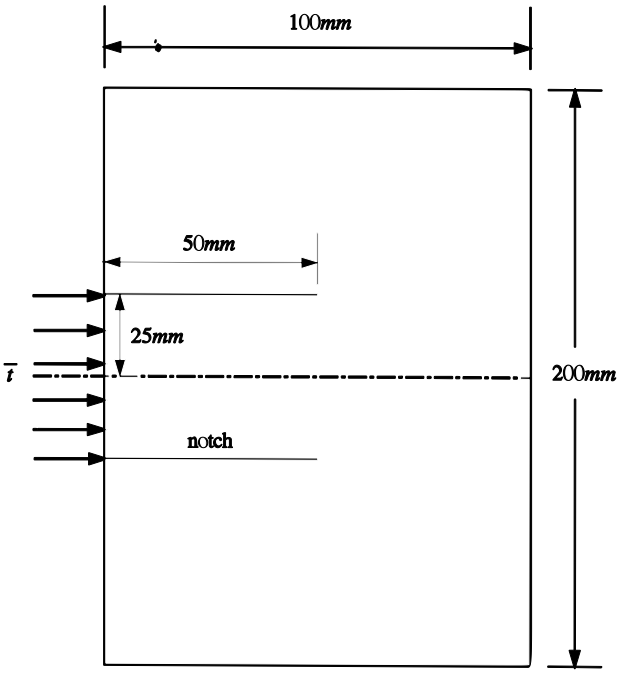

Figure 10 : A schematic sketch of the double edge-notched plate

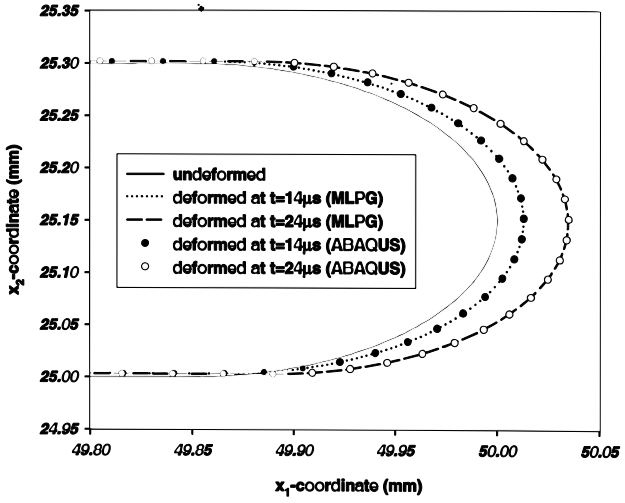

Figure 11 : Undeformed and deformed shapes of the circular notch surface

ential equations are integrated by the backward difference method. The two approximate solutions obtained by the MLPG and the FE methods are compared; the same nodal mesh was used in the two analyses.

Figure 11 displays the undeformed and the deformed shapes of the notch tip. Due to the compressive tractions applied on the edge between the two notches, the notch faces move upwards. It is clear that the two sets of results agree well with each other. The time histories of normal stresses σ_{11} and σ_{22} at the notch tip are plotted in Fig. 12. The dilatational wave arrives at the notch tip at about $7\mu s$. Soon after the arrival of the wave, stresses at the notch

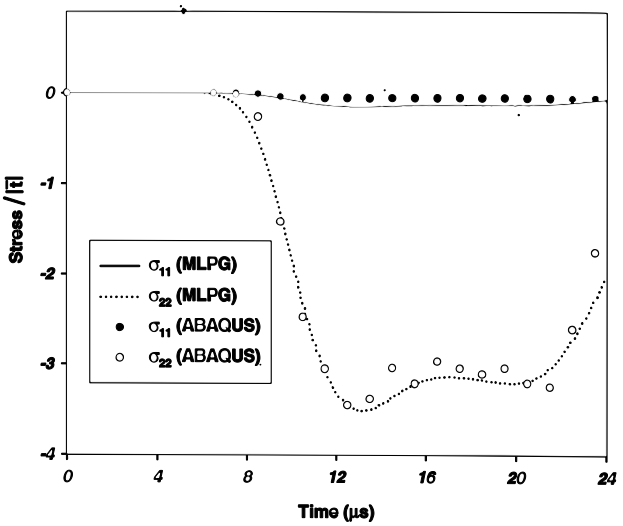

Figure 12 : Time histories of normalized σ_{11} and σ_{22} at the notch tip

tip increase with σ_{22} being significantly larger in magnitude than σ_{11}. For time $t = 14\mu s$ and $24\mu s$, Figs. 13a and 13b evince, respectively, the variations of σ_{22} and σ_{12} at points directly ahead of the notch tip. We note that the axial variation of $|\sigma_{12}|$ exhibits a boundary layer phenomenon near the notch tip; the thickness of the boundary layer equals 0.2% of the length of the notch. The traction free boundary condition at the notch tip requires that $\sigma_{12} = 0$ there. The angular distributions of the principal tensile stress and the maximum shear stress at $t = 14\mu s$ and $24\mu s$ are exhibited in Figs. 14a and 14b. The angular locations, θ, of points where these stresses attain their maximum values are essentially the same at $t = 14\mu s$ and $24\mu s$. Whereas the maximum principal tensile stress occurs at $\theta = 70^\circ$, the maximum shear stress attains its peak value at $\theta = -60^\circ$. These angular positions are close to

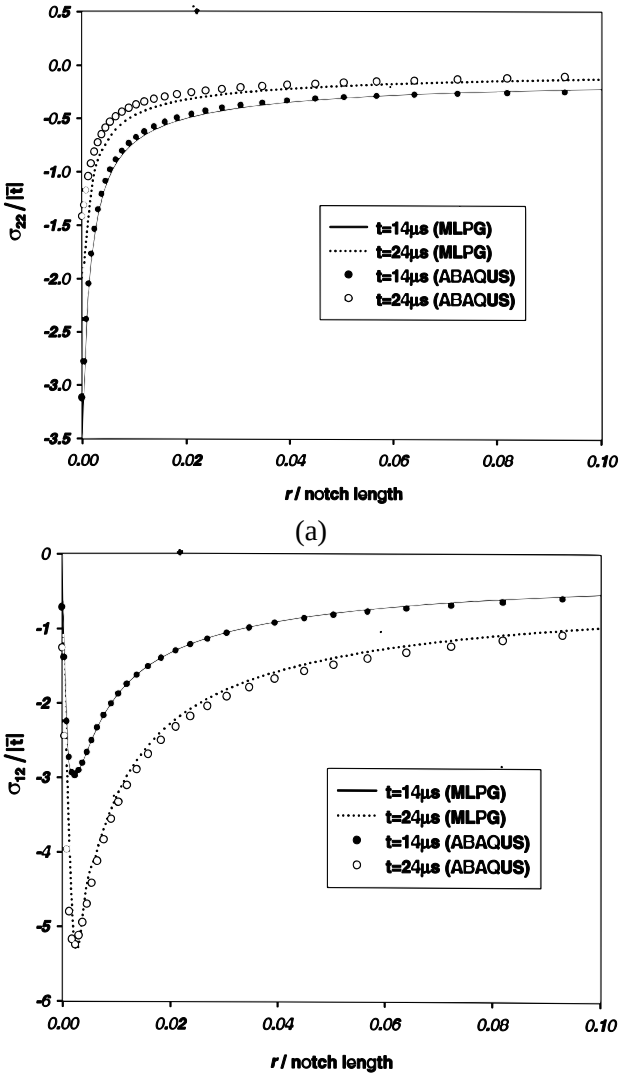

Figure 13 : (a) Variations of normalized σ_{22} with the distance directly ahead of the notch tip (b) Variations of normalized σ_{12} with the distance directly ahead of the notch tip

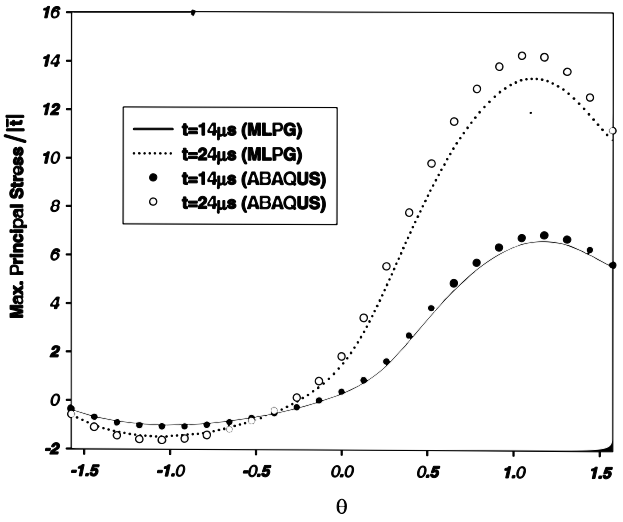

(a)

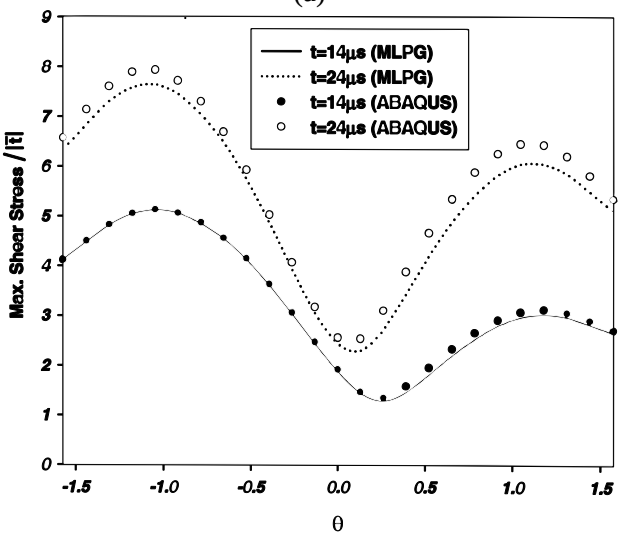

(b)

Figure 14 : (a) Angular distribution of the normalized maximum principal stress on the notch surface at two different times (b) Angular distribution of the normalized maximum shear stress on the notch surface at two different times

those found by Batra and Gummalla (2000) in the transient FE analysis of the thermoviscoplastic problem. Batra and Ravisankar (2000) compared deformation fields computed from the analysis of the 3-dimensional thermoviscoplastic problem with those from the plane strain analysis of the problem. They found that the deformation fields at the midsurface of the plate matched closely with those computed from the plane strain analysis. However, these differed considerably from those on the front and the back surface of the plate where experimental observations are made. The angular distributions of the hoop stress $\sigma_{\theta\theta}$ and the shear stress $\sigma_{r\theta}$ are plotted in Figs. 15a and 15b respectively. Maximum values of $\sigma_{r\theta}$ occur at the extremities of the circular surface of the notch tip, but as noted above, the maximum shear stress is at $\theta = -60^\circ$.

It is clear from the results plotted in Fig. 16a that indeed K_I and K_{II} are proportional to $\sqrt{r}$ during the time interval considered herein. The time histories of the stress intensity factors are depicted in Fig. 16b. Significantly larger values of K_{II} relative to those of K_I imply that the mode-II deformations near the notch tip are dominant. During the time interval $0 \leq t \leq 24\mu s$, K_I is nearly constant but the magnitude of K_{II} increases montonically implying that the mode-mixity parameter does not stay constant. Lee and Freund (1990) modeled the notch as a sharp crack and found that the mode-mixity parameter stays constant till the waves reflected from the right free edge arrive at the crack tip.

We note that the elastostatic analysis of the problem with $\bar{t} = 200MPa\sqrt{mm}$ gave $K_I = -448MPa\sqrt{mm}$ and $K_{II} = -878MPa\sqrt{mm}$. For the elastodynamic problem, the maximum value of $K_I(t)$ during the time interval $0 \leq t \leq 24\mu s$ equals $-275MPa\sqrt{mm}$ but the magnitude of K_{II} continues to increase to $-1150MPa\sqrt{mm}$ at $t = 24\mu s$. The unloading wave reflected from the free right edge of the plate arrives at the notch tip at about $24\mu s$. Thus the static analysis of the problem does not provide a realistic description of the failure mode near a notch tip in a dynamically loaded prenotched plate.

3.3.2 Plate material orthotropic

We now assume that the prenotched plate is made of an orthotropic material with material axes of symmetry coincident with the coordinate axes. Two orthotropic materials, namely orthotropic (1) and orthotropic (2), are considered with the following material properties: orthotropic (1), $E_{11} = 210GPa$, $E_{22} = 0.5E_{11}$, $\nu_{12} = 0.29$,

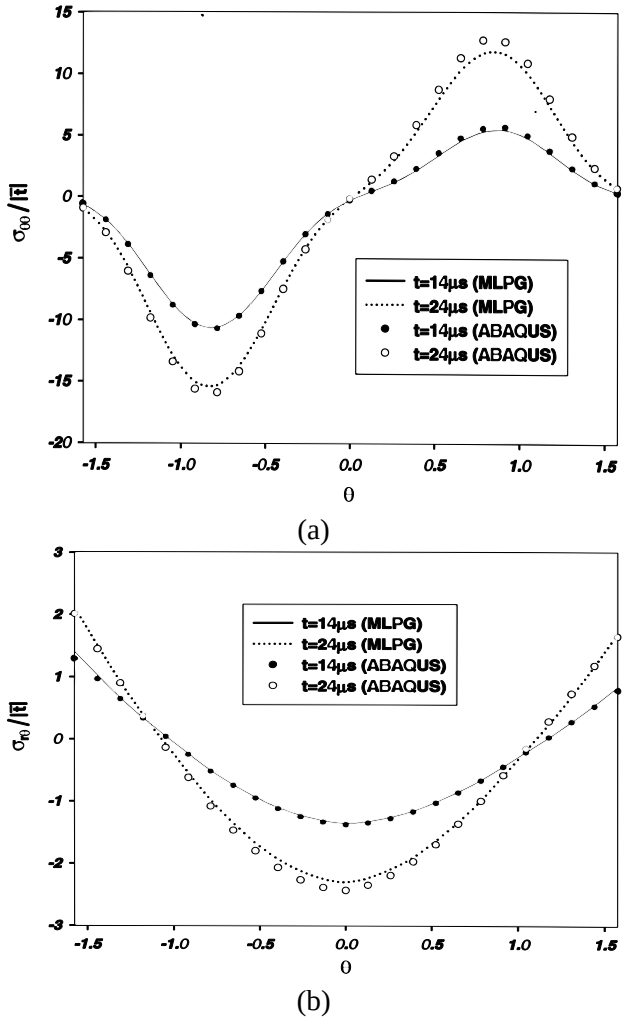

Figure 15 : (a) Angular distribution of the normalized hoop stress on the notch surface at two different times (b) Angular distribution of the normalized shear stress on the notch surface at two different times

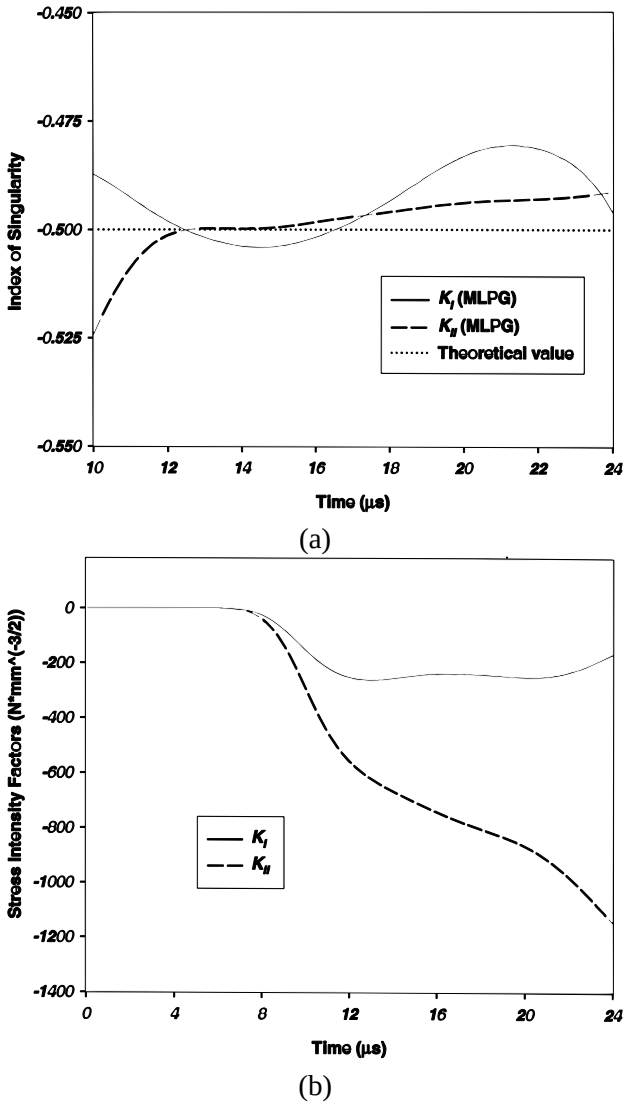

Figure 16 : (a) The time history of the index of singularity for mode I and mode II deformations (b) The time history of the stress intensity factors K_I and K_{II}

$G_{12} = 0.4E_{11}$; orthotropic (2), $E_{11} = 210GPa$, $E_{22} = 0.2E_{11}$, $\nu_{12} = 0.29$, $G_{12} = 0.4E_{11}$. As can be seen from Fig. 17a, subsequent to the arrival of the dilatational wave at the notch tip, the magnitude of the stress intensity factor $K_I(t)$ for orthotropic materials is less than that for the isotropic material. The decrease in the magnitude

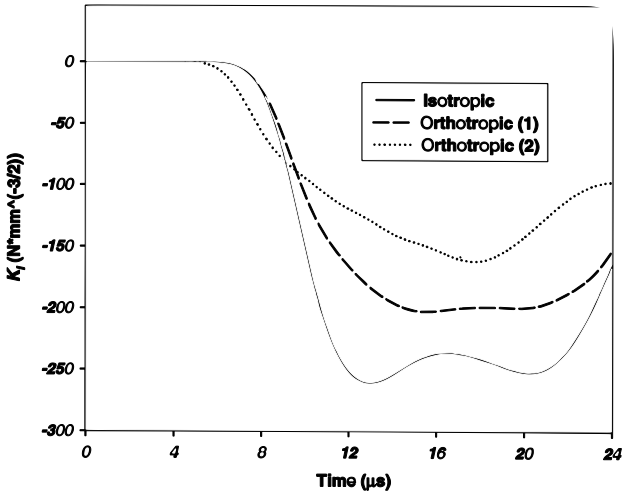

(a)

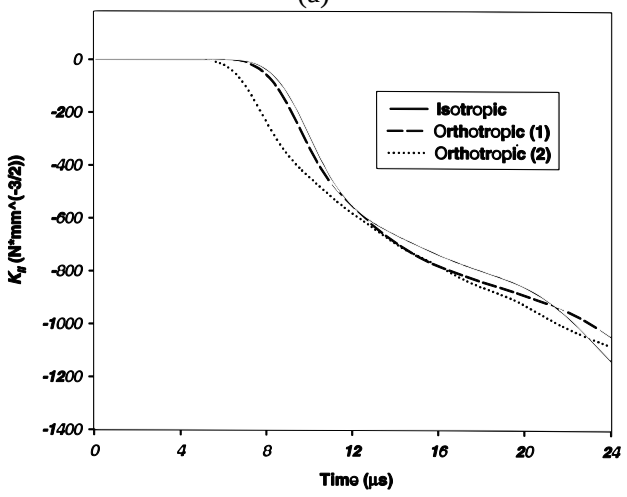

(b)

Figure 17 : (a) The time history of the stress intensity factor K_I for three materials (b) The time history of the stress intensity factor K_{II} for three materials

of $K_I(t)$ is due to the reduction of the Young's moduli of the orthotropic materials in the x_2-direction. However, the time histories of the stress intensity factor $K_{II}(t)$ for isotropic and orthotropic materials in Fig. 17b are almost coincident with each other since the shear modulus G_{12} for these materials has the same value. Thus the mode mixity of the deformation field near the notch tip in an orthotropic plate can be adjusted by suitably modifying the material moduli in the x_1- and x_2-directions.

4 Conclusions

We have used the MLPG method to analyze transient infinitesimal plane strain/stress deformations of an elastic body. The MLPG solution is found to compare very well with the analytical solutions for two problems, namely, wave propagation in a bar, and a rectangular plate with a central crack with plate edges parallel to the crack axis loaded in tension. For the explicit central-difference method, the time step needed to compute the stable solution was found to be much smaller than that given by the stability condition (42); it strongly depended upon the value of the penalty parameter used to satisfy the essential boundary conditions. The computed time histories of the stress intensity factors were found to agree with those available in the literature for the same problem. The MLPG method is then used to analyze transient deformations of a double edge prenotched plate with the smooth edge between the two notches loaded by uniformly distributed compressive tractions. The deformations and stress fields near the notch tip computed by the MLPG method agree well with those obtained from the finite element solution. It is found that the variation of the shear stress σ_{12} with the distance r ahead of the notch tip exhibits a boundary layer effect. Outside of this boundary layer region, stresses exhibit the $1/\sqrt{r}$ singularity. The mode mixity of the deformation field near the notch tip in an orthotropic plate can be adjusted by modifying values of the in-plane material moduli.

Acknowledgement: This work was partially supported by the Office of Naval Research grant N00014-98-1-0300 to Virginia Polytechnic Institute and State University with Dr. Y.D.S. Rajapakse as the program manager.

References

Anderson T.L. (1995): Fracture Mechanics - Fundamentals and Applications, CRC Press, Boca Raton.

Atluri S.N. and Zhu T. (1998): A New Meshless Local Petrov-Galerkin (MLPG) Approach in Computational Mechanics. *Computational Mechanics*, Vol. 22, pp. 117-127.

Atluri S.N., Kim H.G. and Cho J.Y. (1999): A Critical Assessment of the Truly Meshless Local Petrov-Galerkin

(MLPG), and Local Boundary Integral Equation (LBIE) Methods. *Computational Mechanics*, Vol. 24, pp. 348-372.

Atluri S.N. and Zhu T. (2000): The Meshless Local Petrov-Galerkin (MLPG) Approach for Solving Problems in Elasto-statics. *Computational Mechanics*, Vol. 25, pp. 169-179.

Atluri S.N. and Shen S.P. (2002a): The Meshless Local Petrov-Galerkin (MLPG) Method: A Simple & Less-costly Alternative to the Finite Element Methods. *Computer Modeling in Engineering & Sciences*, Vol. 3(1), pp. 11-51.

Atluri S.N. and Shen S.P. (2002b): The Meshless Local Petrov-Galerkin (MLPG) Method, Tech Science Press, California, 430 pages.

Baker B.R. (1962): Dynamic Stresses Created by a Moving Crack. *Journal of Applied Mechanics*, Vol. 29, pp. 449-455.

Batra R.C. and Gummalla R.R. (2000): Effect of Material and Geometric Parameters on Deformations near the Notch Tip of a Dynamically Loaded Prenotched Plate. *International Journal of Fracture*, Vol. 101, pp. 99-140.

Batra, R.C. and Ravisankar, M.V.S. (2000): Three dimensional numerical simulation of the Kalthoff Problem. *International Journal of Fracture*, Vol. 105, pp. 161-186.

Ching H.K. and Batra R.C. (2001): Determination of Crack Tip Fields in Linear Elastostatics by the Meshless Local Petrov-Galerkin (MLPG) Method. *Computer Modeling in Engineering & Sciences*, Vol. 2(2), pp. 273-289.

Fedelinski P., Aliabadi M.H. and Rooke D.P. (1994): The Dual Boundary Method: J-integral for Dynamic Stress Intensity Factors. *International Journal of Fracture*, Vol. 65, pp. 369-381.

Gu Y.T. and Liu G.R. (2001): A Meshless Local Petrov-Galerkin (MLPG) Method for Free and Forced Vibration Analyses for Solids. *Computational Mechanics*, Vol. 27, pp. 188-198.

Kalthoff J.F. and Winkler S. (1987): Failure Mode Transition at High Rates of Shear Loading, in Chiem C.Y., Kunze H.D., and Meyer L.W. (eds.). *Impact Loading and Dynamic Behavior of Materials*, Verlag, Vol. 1, pp. 185-195.

Lancaster P. and Salkauskas K. (1981): Surfaces generated by moving least squares methods. *Mathematics of Computation*, Vol. 37, pp. 141-158.

Lee, Y.J. and Freund, L.B. (1990): Fracture initiation due to asymmetric impact loading of an edge cracked plate. *Journal of Applied Mechanics*, Vol. 57, pp. 104-111.

Lin H. and Atluri S.N. (2000): Meshless Local Petrov-Galerkin (MLPG) Method for Convection-diffusion Problems. *Computer Modeling in Engineering & Sciences*, Vol. 1(2), pp. 45-60.

Long S. and Atluri S.N. (2002): A Meshless Local Petrov-Galerkin Method for Solving the Bending Problem of a Thin Plate. *Computer Modeling in Engineering & Sciences*, Vol. 3(1), pp. 53-64.

Miannay D.P. (2001): Time-Dependent Fracture Mechanics. Springer-Verlag Inc., New York.

Newmark N.M. (1959): A Method of Computation for Structural Dynamics. *J. Eng. Mech. Div., Proc. ASCE*, Vol. 85, No. EM3, pp. 67-94.

Nishioka T. and Atluri S.N. (1980): Numerical Modeling of Dynamic Crack Propagation in Finite Bodies by Moving Singular Elements, Part II. *Journal of Applied Mechanics*, Vol. 47, pp. 577-582.

Organ D.J., Fleming M. and Belytschko T. (1996): Continuous Meshless Approximations for Nonconvex Bodies by Diffraction and Transparency. *Computational Mechanics*, Vol. 18, pp. 225-235.

Warlock A., Ching H.K., Kapila A.K. and Batra R.C. (2002): Plane Strain Deformations of an Elastic Material Compressed in a Rough Rectangular Cavity. *International Journal of Engineering Science*, Vol. 40, pp. 991-1010.